Materials Research. 2024; 27(suppl 2):e20240201
DOI: https://doi.org/10.1590/1980-5373-MR-2024-0201

$CaTiO_3$: Influence of Ag Doping on Photocatalytic Activity for Application in Rhodamine B dye Removal

***Flávia Landgraf Cuzzati*[a] , *Gustavo Aparecido Silva Parras*[a], *Gabriela de Souza Freitas*[a],**

***Marcela Prado Silva Parizi*[a*], *Agda Eunice de Souza*[a]**

[a]*Universidade Estadual Paulista (UNESP), Presidente Prudente, SP, Brasil.*

Received: April 30, 2024; Revised: June 25, 2024; Accepted: July 01, 2024

This study focuses on the preparation and characterization of silver-doped calcium titanate ($CaTiO_3$) photocatalysts for the degradation of Rhodamine B (RhB) dye. Utilizing a hydrothermal microwave-assisted method, efficient photocatalysts of pure $CaTiO_3$ (CT) and 3% (CT3%) and 5% (CT5%) Ag-doped $CaTiO_3$ were prepared. X-ray diffraction confirmed the orthorhombic phase of $CaTiO_3$ with residual TiO_2, more pronounced in the CT3%. Micro-Raman and FTIR spectra verified the presence of TiO_2, while SEM images revealed distinctive morphologies. The band gap energy was lower in Ag-doped samples, particularly in the CT3% sample. Photocatalytic tests demonstrated superior RhB degradation with the CT3% catalyst. A 2^2 factorial design was used to determine the ideal condition for the photocatalysis. Photocatalysis with CT3% was efficient in toxicity removal, but stability tests indicated a decline in performance over multiple cycles. These findings suggest the potential of Ag-doped $CaTiO_3$ as efficient photocatalysts for dye degradation.

Keywords: *Silver-doped calcium titanate, Hydrothermal microwave-assisted method, Photocatalysis, Rhodamine B, Dye.*

1. Introduction

In recent years, wastewater contaminated with dyes has been the focus of study, particularly regarding processes and materials that demonstrate efficacy in degrading or removing these pollutants. In general, dyes in wastewater originate from industries such as leather, paper, textile, or clothing. There are reports in the literature that approximately 20% of the dyes used by textile industries, for example, are disposed into wastewater streams, and up to 10% of the dyes used in the paper and leather industries are lost as waste[1]. Rafiq et al.[2] mentions several strategies reported in the literature that have been evaluated as potential solutions for dye removal from contaminated water. The authors mention, for example, biological and/or aerobic treatments, coagulation, adsorption, catalysis, and photocatalysis, among others. Among these processes, heterogeneous photocatalysis is effective, depending on the catalyst used. Photocatalysis constitutes a segment of advanced oxidative processes (AOPs), which generally involve a hydroxyl radical (•OH) as the main oxidizing agent. In photocatalysis, the presence of UV radiation, whose energy is higher than the band gap energy of the catalyst, accelerates the reaction on the catalyst surface, generating excitons (electron-hole or e^- and h^+ pairs) which, in turn, interact with molecules adsorbed on the surface. Electrons (e^-), for instance, can reduce adsorbed chemical species, while holes (h^+) can oxidize other chemical species[3].

Heterogeneous photocatalysis is preferred over homogeneous photocatalysis for practical applications due to the ease of separating the catalyst from the reaction mixture, which reduces contamination and offers both environmental and economic benefits. Heterogeneous photocatalysis is therefore closely related to the characteristics of the catalyst material, such as its crystalline structure and electronic states. In terms of materials, photocatalysts can be grouped into metallic oxides, metallic sulfides, metallic nitrides, metallic hydroxides, bismuth-based salts, carbon-based polymers, silver halides (Ag), perovskites, and other new materials such as metal-organic structures and covalent organic structures[4].

Among photocatalytic materials, semiconductors have received special attention due to their band gap characteristics that can generate excitons capable of participating in the redox reaction of pollutants. Numerous studies in the literature have shown interest in the heterogeneous photocatalysis of TiO_2 in organic compounds, such as dyes. Photocatalysis studies have been conducted with TiO_2 pure[5], doped[6], composites, or heterostructures form[7]. In addition to TiO_2, several studies have shown the efficiency of various other semiconductors in the photocatalytic process of different contaminants, such as zirconates[8], titanates[9], tungstates[10], and so on.

Calcium titanate ($CaTiO_3$), an n-type semiconductor with perovskite structure (ABO_3), is cited in the literature as a promising photocatalyst alternative to TiO2 due to its wider band gap energy (~3.6 eV) and unique properties that favor its use in heterogeneous photocatalysis, whereas the band gap of TiO_2 is around 3.2 eV according to the literature[11]. Furthermore, dopants can also be accommodated in the perovskite structure, promoting desired defects or oxygen

*e-mail: marcela.prado@unesp.br

excess, which significantly contributes to its catalytic performance[12].

There are studies in the literature evaluating the photocatalytic potential of pure $CaTiO_3$[13,14], doped[14,15], co-doped[16,17], in composite formats[18], and heterojunctions[19,20], prepared by various synthesis methods[12]. However, there are no previous studies on $CaTiO_3$ doped exclusively with Ag at the A-site of its perovskite structure. The introduction of Ag as a dopant, as explored in this study, induces the formation of local defects within the perovskite lattice. These defects result in distortions within the electronic structure of the lattice ions, creating intermediate states within the band gap. The emergence of these interband states effectively reduces the band gap energy, a beneficial outcome for photocatalytic processes[4]. This reduction facilitates the absorption of a broader spectrum of visible light, thereby promoting the generation of excitons (electron-hole pairs) crucial for enhancing redox reactions that degrade dyes. Essentially, this modification can enhance the production of reactive species during the photocatalytic process.

In this context, this work presents results from a study on the photocatalytic activity of pure $CaTiO_3$ and Ag-doped $CaTiO_3$ prepared by the microwave-assisted hydrothermal method. In this study, we aim to investigate the influence of the dopant on the perovskite structure and the morphological characteristics of the photocatalyst in the photocatalytic degradation of synthetic dye. Furthermore, this research aligns with the objectives of sustainable development (SDGs), specifically the goal *Clean Water and Sanitation* and the goal *Life Below Water*.

2. Materials and Methods

2.1. $CaTiO_3$ preparation and characterization

$CaTiO_3$ (CT) was prepared by the microwave-assisted hydrothermal method (Figure 1). For this, 0.01 mol of the CT compound was prepared using calcium chloride ($CaCl_2.H_2O$) and titanium oxide (TiO_2) as precursors, diluted in 15 mL of hydrogen peroxide (H_2O_2) heated at 60°C under stirring for ~15 min, using a Teflon® cup (capacity of 100 mL). Then, 50 mL of NaOH was added to the solution, and it was kept stirring (at 60°C) for an additional 40 min. Next, the cup containing the solution was placed in a hermetically sealed container, also made of Teflon®, and placed in a household microwave oven adapted with a timer, temperature controller, and heating ramp. The synthesis proceeded with a heating ramp of $10°C min^{-1}$ up to 140°C for 40 minutes. At the end of the reaction time, the system was naturally cooled to room temperature, washed with deionized water until reaching a neutral pH (~7), and dried in an oven at 100°C for 24 hours. This procedure was repeated for the preparation of Ag-containing $CaTiO_3$. In this case, proportions of 3% and 5% mol of silver nitrate ($AgNO_3$) were added to the solution containing the CT precursors immediately after the addition of $CaCl_2.H_2O$, before being subjected to microwave heating. These samples were called CT3% and CT5%.

The ceramic powders were characterized by X-ray diffraction (Shimadzu, model XRD-6000), using $CuK_{\alpha 1}$ ($\lambda = 1.5406Å$) and $CuK_{\alpha 2}$ ($\lambda=1.5444Å$) radiation source, with a voltage of 40 kV and current of 30 mA, scanning from 10° to 80° (2θ) at a rate of $2°min^{-1}$; Raman spectroscopy (Renishaw, inVia), coupled with a Leica microscope (50x objective and spatial resolution of $1 \mu m^2$) and a CCD detector; FTIR spectroscopy using Perkin Elmer Frontier instrument equipped with a diamond attenuated total reflection (ATR) module. The FTIR spectra were recorded in the range of 4000 to 250 cm^{-1} at a scan rate of one spectrum per 64 s with a resolution of 2 cm^{-1}, at 298 K; Scanning electron microscopy (Carl Zeiss, EVO LS15), where the ceramic powders were deposited on carbon tape and coated with Au via sputtering; Absorption in the UV-Vis region, using Shimadzu UV-1800 spectrophotometer with a sphere of integration using $BaSO_4$ as a blank.

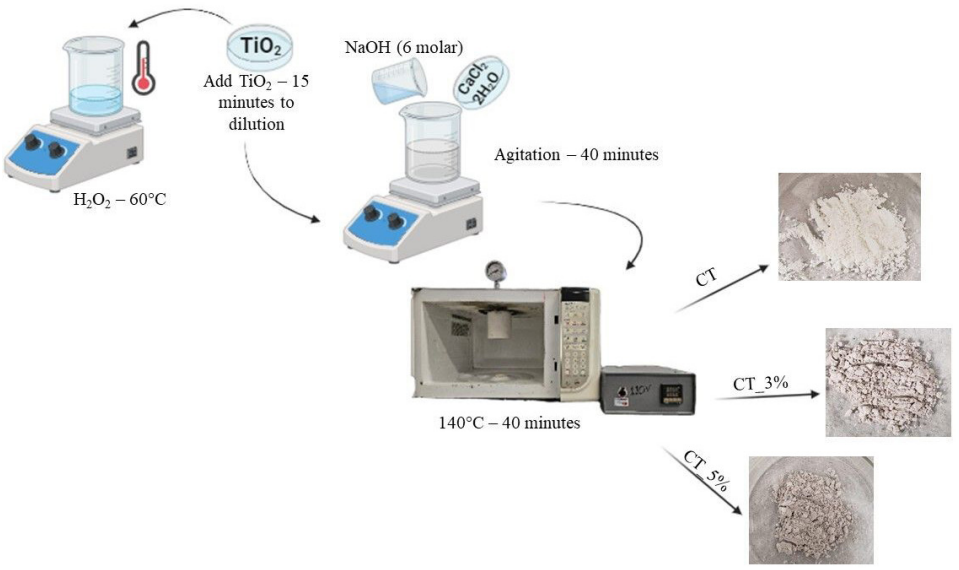

Figure 1. Schematic representation of the $CaTiO_3$ and Ag-containing $CaTiO_3$ preparation.

2.2. $CaTiO_3$ photocatalysis

2.2.1. Photodegradation degradation experiments

To investigate the photocatalytic degradation process control experiments were conducted: adsorption and photolysis.

Adsorption experiments were performed in the dark, solutions containing 10 mg L^{-1} of RhB and 1g L^{-1} of photocatalyst (CT, CT3% or CT5%) were placed in flasks of 50 mL at 25 °C, in a shaker (Lucadema, Luca-222), for 120 min.

Photolysis experiments were conducted using the experimental setup illustrated in Figure 2, equipped with two 8 W lamps (Philips) emitting UVC radiation with a peak at 254 nm. The temperature was maintained constant at 25°C by a thermostat bath connected to the reaction beaker, wherein the solution was kept in continuous agitation by magnetic stirring. In photolysis experiments, a solution containing 10 mg L^{-1} of RhB was irradiated for 120 minutes and aliquots were collected at predefined times and analyzed to evaluate [RhB].

Finally, in photocatalysis processes, solutions containing 10 mg L^{-1} of RhB and 1g L^{-1} of photocatalyst (CT, CT3% or CT5%) were placed in the reaction beaker of the experimental setup (Figure 1) and irradiated for 120 min. Samples were taken at 0, 5, 15, 30, 60, 90, and 120 minutes, centrifuged (3000rpm/2min), and analyzed by UV–vis spectrophotometer (Agilent Cary 60 UV-Vis) at λ = 552 nm, to determine RhB concentration. All experiments were performed in triplicates.

2.2.2. Experimental design

To determine the ideal condition for RhB removal by photocatalysis, a factorial design at two levels of each variable (2^2)[20] was employed. The independent variables of the process were $[RhB]_0$ (50 or 100 mgL^{-1}) and $[CT]_0$ (1 or 2 gL^{-1}), while the response variable was the percentage removal of RhB after 120min of photocatalysis (% RhB removal). All experiments were conducted in duplicate.

The optimal values for photocatalyst dosage and RhB concentration, which resulted in the highest RhB degradation (analyzed via %RhB removal), were determined through response surface methodology[21], using STATISTICA 7.0 software.

2.2.3. Toxicity assays

The best operating conditions obtained from the analysis of the factorial design were selected to perform the toxicity test. The toxicity of the samples was tested using the method described by Fiskejö[22] and adapted by Salazar Mercado et al.[23]. Recent studies confirm the effectiveness of toxicity analysis using the species Lens culinaris, primarily due to it being a new, cost-effective, and quick alternative[24,25].

In this study, the germination of Lens culinaris seeds was conducted in Petri dishes, with filter paper used as substrates. The seeds were kept in the dark for 5 days at a temperature of 20 °C, with a contaminant solution ratio of 1:3 w/v. The negative control was performed using distilled water.

Phytotoxicity was analyzed by the germination index, determined by the number of germinated seeds (NGS), where the root grew more than 5 cm, relative to the total number of seeds (TNS), using Equation 1.

$$GI(\%) = \frac{NSG}{NST}.100 \quad (1)$$

The mitotic index (MI) was determined by examining meristematic cells under a microscope and staining them with the Panótico Rápido kit. About 100 cells per sample were observed, and Equation 2 was utilized, with NDC representing the total number of dividing cells and TNC indicating the total number of cells analyzed.

$$MI(\%) = \frac{NDC}{TNC}.100 \quad (2)$$

2.2.4. CT3% recycling

To assess the reuse of CT3%, the optimal operational conditions derived from the factorial design analysis were chosen. Following the initial cycle, the solution was centrifuged (3000 rpm/2 min), and the photocatalyst was reintroduced into the reactor. This process was repeated four times.

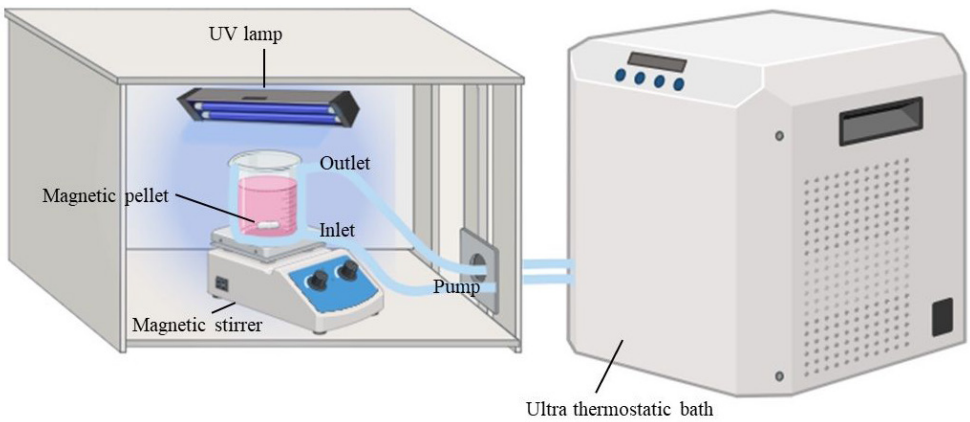

Figure 2. Simplified diagram of the apparatus used in the photocatalysis experiments.

3. Results

3.1. $CaTiO_3$ characterization

The X-ray diffraction results of the titanate samples are shown in Figure 3. In all samples, the orthorhombic phase of $CaTiO_3$ (JPCDF 89-8033) was identified. However, it can be observed that there was precipitation of secondary phases, such as rhombohedral-structured $CaCO_3$, for example, identified in all samples, with less evidence in the CT5% sample. According to Ücker et al.[20], the use of water as a reaction medium contributes to this phase formation in perovskites. According to the authors, CO_2 in an aqueous medium forms an HCO_3^- molecule that interacts with Ca during the hydrothermal reaction, forming the $CaCO_3$ phase.

The presence of residual TiO_2 phase (anatase, tetragonal) was also observed in both samples containing Ag (CT3% and CT5%). It is noted that the presence of TiO_2 is more evident for the sample Ag-doped 3mol%, which is associated with the lower crystallinity of the main CT phase, characterized by the decrease in the intensities of characteristic peaks. Silver (Ag) was not identified in the diffractograms due to its low doping content. However, a slight peak shift around $2\theta = 33°$ towards smaller angle values was observed, which may be associated with the presence of Ag in the CT host lattice. Lee et al.[26] found similar results, where Ag+, added via the photoreduction method, may have been distributed homogeneously on the $CaTiO_3$ surface, according to the authors.

Figure 4 shows the micro-Raman spectra of the titanate. For the CT sample, all Raman modes are attributed to the orthorhombic perovskite phase without the presence of Ag, according to the literature[27-30]. The nine Raman modes observed in the range from 177 to 808 cm^{-1} are attributed to $CaTiO_3$ orthorhombic structure and are also by other studies, within a narrow range of shifts that vary according to the method used in the compound preparation[26]. The bands at 177, 224, 244, 285, and 337 cm^{-1} are attributed to the O–Ti–O bending modes. The bands in the region from 224 to 337 cm^{-1} correspond to modes associated with oxygen atom chain rotation. The bands at 462 and 537 cm^{-1} characterize the Ti–O torsional mode (internal bending or vibration of the oxygen chain), and at 660 cm^{-1}, it refers to the symmetric stretching vibration of Ti–O, suggesting the distortion of the titanium octahedra in the $CaTiO_3$ perovskite structure[20,27,29,31]. It is noted that some of these bands repeat for the CT3% and CT5% samples, showing the presence of vibrational modes of the orthorhombic phase of $CaTiO_3$. In these samples, there are also some vibrational modes (143, 197, 396, 515, and 640 cm^{-1}) corresponding to the presence of TiO_2 in the anatase phase[32], as identified in the X-ray diffraction pattern of these samples. The band at 691 cm^{-1}, evident only in the CT5% sample, may be related to the presence of Ag in the perovskite structure, while the band at 1084 cm^{-1}, present in the CT sample, is related to the calcium carbonate ($CaCO_3$ - calcite)[33,34].

Figure 5 shows the FTIR spectra of the titanate samples. Generally, for perovskite-structured titanates, the peaks between 500 and 900 cm^{-1} correspond to metal-oxygen bonds. The peaks at 529 cm^{-1} and 882 cm^{-1}, observed in the CT sample, may characterize the vibrational modes of stretching and bending of the Ti–O bond within the [TiO_6] octahedron cluster of the perovskite structure[20,35]. With the Ag-doping, a slight shift is observed in the wavenumber corresponding to the vibrational bending mode at 882 cm^{-1}. This may be associated with the partial substitution of Ca/Ag in the perovskite lattice. Since Ag^{1+} has a smaller ionic radius than Ca^{2+}, there is a reduction in the perovskite unit cell volume, resulting in small variations in the Ti–O interaction, which leads to the shift in the wavenumber of the absorption corresponding to this bond. It can also be observed that there is a well-defined peak at 404 cm^{-1} in the CT3% sample, which possibly corresponds to the Ti–O vibrations of the TiO_2 phase quite evident in this sample.

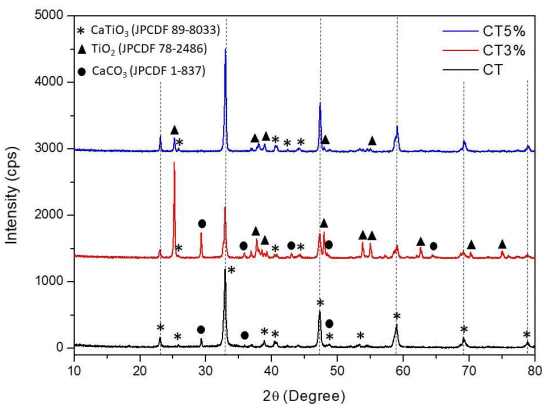

Figure 3. X-ray diffraction patterns of CaTiO3 samples CT, CT3% and CT5%.

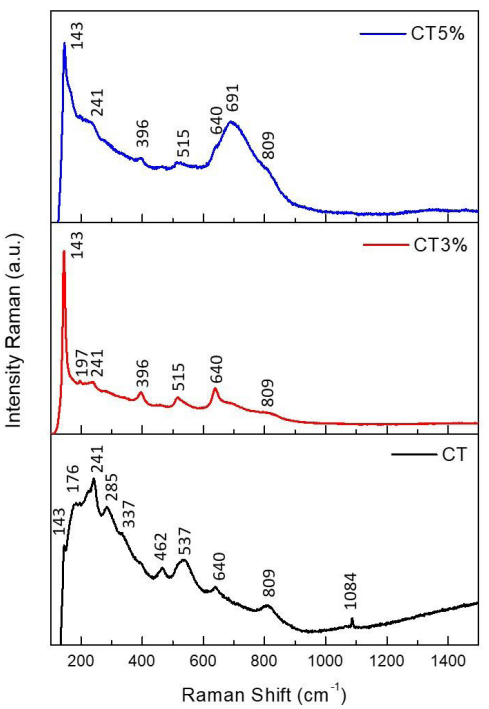

Figure 4. Raman spectra of CT, CT3%, and CT5% samples.

The peak at 1408 cm^{-1} observed in the CT sample may indicate vibrational modes of symmetric stretching of the Ca–O–Ca bond[35]. With the Ag-dopant addition, a decrease and shift of this band are noted, evidencing the Ag/Ca substitution in the perovskite structure. The broad peak at 3404 cm^{-1} is characteristic of O–H bonds, indicating the presence of hydration water possibly adsorbed onto the particle surface or, when combined with the peak at 1649 cm^{-1}, may also indicate defects caused by OH^- groups in the titanate lattice, originating from the use of the NaOH mineralizer during the synthesis process[36,37].

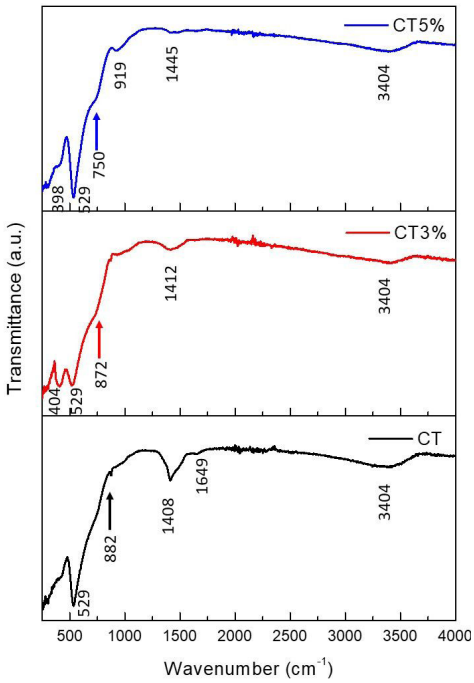

Figure 5. FTIR spectra of CT, CT3%, and CT5% samples.

Figure 6 shows the SEM images of the titanate powders. It can be observed that in the CT sample without the dopant (Figure 6a), some particles exhibit a spherical morphology, while others show a tendency to form edges, generating architectures close to cubes or cuboids, with sizes not exceeding 1 µm. Other works in the literature have also shown CT particles with cubic geometry, however, larger than 1 µm. These slight variations may be associated with different synthesis methods and even the precursors used[20,31,38]. It is also possible to observe that many particles are formed from the smaller adjacent particles agglomeration, which leads to considering a self-assembly process, that is, a spontaneous self-organized growth[39], as already observed in previous works[40,41]. With the 3 and 5 Ag-mol% addition (Figure 6b and 6c), respectively), it can be observed that the morphology of the particles assumes a cubic and prismatic geometric configuration, with well-defined edges. Some of them exhibit overlapping faces, indicating the formation of mesocrystals, whose growth process by oriented attachment in self-organization is also considered, as the particles show surfaces with stacking faults[20]. It is worth noting that the presence of OH^- groups on the perovskite crystals surface, originating from the synthesis process, can act as ligands and

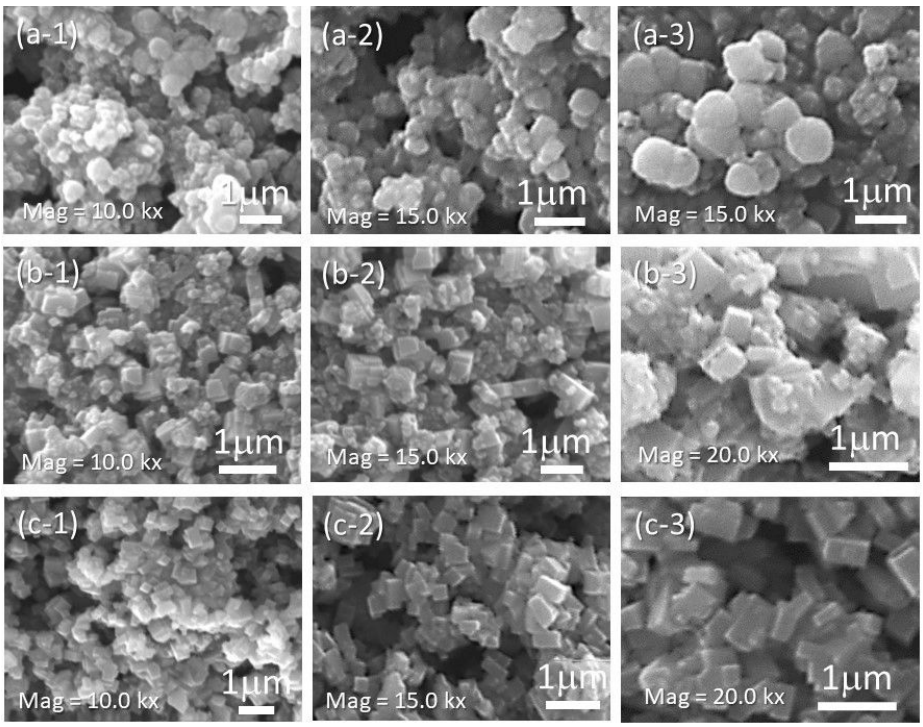

Figure 6. SEM images of titanate samples: (a) CT; (b) CT3%; (c) CT5%.

contribute to the existence of a driving force that leads to the self-assembly process between the materials nanocrystals[39,42,43]. The larger morphology definition for these samples may be associated with both the Ag presence in the $CaTiO_3$ matrix, where charge imbalance could contribute to the driving force for morphological formation, and the TiO_2 residual, identified by XRD. In this case, there is a possibility of $CaTiO_3$-TiO_2 heterojunction forming, due to similarities between their crystal structures and band structures, as observed by Lin et al.[44]. Both the Ag and the potential heterostructure formation contribute to alterations in the properties exhibited by the material, including photocatalysis.

Figure 7 shows the band gap of pure CT and Ag-doped CT. The Eg values were determined using the Wood and Tauc method[45] according to Equations 3 and 4. In these equations, *h* is Planck constant, ν is the frequency of the radiation (UV-Vis), *n* indicates the type of electronic transition between bands (indirect transition (n = 2) for $CaTiO_3$), α is a constant, or absorption coefficient, which was determined based on the reflectance (*R*) of the opaque material. To compute the Eg, the linear part of $(\alpha h\nu)^{1/n} \times h\nu$ was extrapolated to the point α equal to zero.

$$h\nu\alpha = \left(h\nu - E_g\right)^n \tag{3}$$

$$\alpha = \frac{\left(1 - R_\infty\right)^2}{2R_\infty} \tag{4}$$

It is observed that the highest band gap value for CT was 3.52 eV, consistent with values found for this perovskite[17,46]. Upon adding 3 Ag-mol% to the CT host lattice, a decrease in the band gap to 3.25 eV is observed. This decrease may be associated with deviations from the orthorhombic crystal structure caused by the substitution of Ca^{2+} by Ag^{1+}, which consequently induces defects in the valence and conduction bands. This decrease in the band gap value may be related to the Burstein-Moss effect, a phenomenon observed in semiconductors when the concentration of free carriers is increased[14]. In other words, the substitution of Ca^{2+} by Ag^{1+} destabilizes charges at the isomorphic substitution site, contributing to an increase in the carrier number. Furthermore, the decrease in Eg can enhance some material properties, such as photocatalysis, as less energy is required to promote excitons. It is important to note that in the CT3% sample, there is also the simultaneous presence of the TiO_2 phase, as observed in the XRD results (Figure 3). This phase may therefore assist in altering the Eg of this sample if there is a $CaTiO_3$-TiO_2 heterojunction, whose band gap is 3 eV approximately. In this case, defects arise from the interface between phases and/or crystals, which may result, for example, in oxygen vacancies[47]. For the CT5% sample, a slight increase in the Eg value is observed, although still lower than the undoped sample. Again, this behavior may be associated with both Ca/Ag substitution and the presence of the TiO_2 phase in this sample, apparently with lower crystallinity, as discussed in the XRD results.

It is also observed, in all absorption spectra, that there is an exponential decay in the lower absorption region (tail), indicating the localized states within the band gap. This absorption edge indicates a degree of structural order-disorder in the titanate lattice, including short, medium, and long distances, which contributes to changes in band gap energy, a result in agreement with the previously discussed data[41].

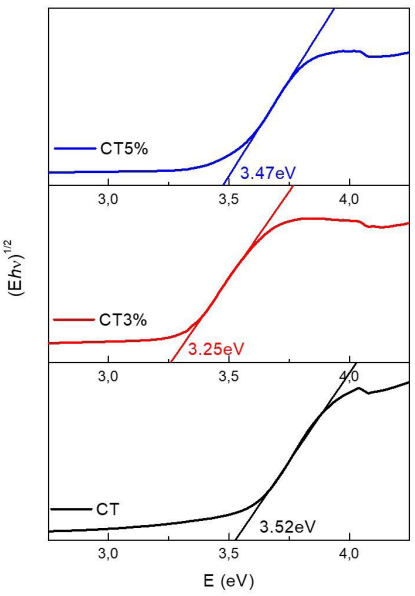

Figure 7. UV-Vis absorbance spectra as a function of the energy of CT, CT3%, and CT5% samples.

3.2. Photocatalytic activity

The control experiments (adsorption and photolysis assays) demonstrated that there was no variation in the concentration of RhB throughout the experiments. This outcome reveals that the photocatalysts under study (CT, CT3%, or CT5%) do not adsorb the dye rhodamine B under the studied conditions. Additionally, it is revealed that the dye RhB does not undergo photolysis within two hours under UV radiation at 254 nm. These findings indicate that the degradation of the dye in the photocatalysis experiments results exclusively from the reactions initiated by the photocatalysts.

Figure 8 presents the results of the photocatalysis experiments with the three studied photocatalysts. Photodegradation using $CaTiO_3$ was found to be incapable of removing the RhB dye after 120 minutes of UV irradiation at 254 nm. The observed result can be attributed to the limitation in $CaTiO_3$ overall photocatalytic effectiveness despite its high photoactivity, owing to its wide bandgap and low quantum efficiency. An important factor contributing to this limitation is the ultrafast recombination of photoexcited electron-hole pairs[48].

Conversely, photocatalysis with CT5% exhibited a 15% removal of RhB after 120 minutes of degradation, and photocatalysis with CT3% demonstrated excellent performance in RhB removal, achieving 99% degradation after 120 minutes of irradiation.

The superior performance of the CT3% photocatalyst is consistent with the results presented in Figure 6, which show a lower band gap value for the CT3% sample compared to the photocatalysts CT and CT5%. Additionally, the XRD results

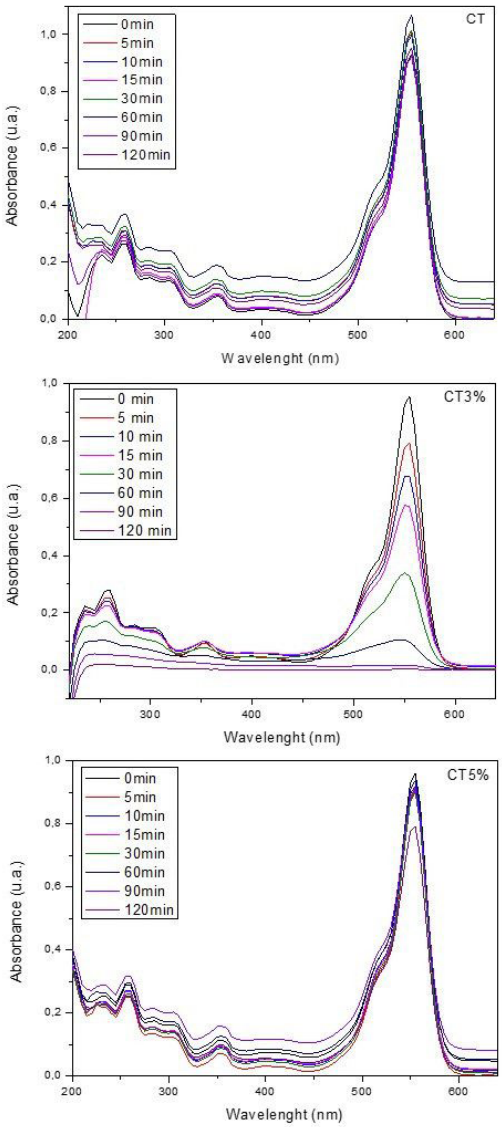

Figure 8. The variation in UV–visible absorption spectra of Rhodamine B (RhB) dye solution as a function of irradiation time in the presence of pure CT, CT3%, and CT5%, as a catalyst under UV light radiation.

also reveal that in the CT3% samples, there is a simultaneous presence of the TiO_2 phase, which may assist in altering the Eg of this sample if there is a $CaTiO_3$-TiO_2 heterojunction.

Passi and Pal[49] also observed superior photocatalytic performance with $CaTiO_3$ modified with 3% Ag compared to 5%. They attributed this to the decrease in band gap energy values, which were found to be lower than those of pure CT. The reduction in band gap upon modification with Ag was linked to a decrease in the extent of recombination of photo-generated charge carriers. However, it was observed that this reduction in band gap occurred only up to 3%; increasing the loading amount of Ag to 5% increased the band gap. This phenomenon may be attributed to the excessive loading of metal nanoparticles, which act as recombination centers and influence the band gap. The authors also observed a maximum decrease in band gap energy in the case of the CT3% sample.

The experimental results suggest that the degradation capacity of $CaTiO_3$ is significantly enhanced by depositing Ag on its surface, with higher RhB removal percentages for the CT3% and CT5% photocatalysts compared to pure CT. These metallic deposits act as electron accumulation sites, effectively capturing photoexcited electrons from the $CaTiO_3$ surface and transferring them to oxygen molecules, consequently generating more reactive intermediate species, such as highly reactive hydroxyl radicals (•OH) and superoxide radical anions ($•O_2^-$), which can react with RhB, resulting in increased degradation[49].

3.3. Main influencing effects on RhB degradation in UV photocatalysis/$CaTiO_3(Ag_{3\%})$: experimental design approach

An experimental design 2^2 was conducted to identify optimal conditions and elucidate the variables most influential in the degradation process of the RhB dye by photocatalyst CT3%. Table 1 shows the experimental design matrix used, where $[RhB]_0$ and $[CT3\%]_0$ were used as independent variables, while RhB removal percentage was the dependent variable.

According to Table 1, the ideal condition for the RhB removal was $[RhB]_0$=100 mgL^{-1} and $[CT3\%]_0$= 1 g L^{-1}.

Figure 9 presents the Pareto diagram derived from the factorial design and reveals insights into the influence of the investigated variables on the degradation process. Remarkably, the [RhB] emerges as the most impactful variable, with a significant positive effect, indicating its strong contribution to degradation efficacy. Next, the interaction between variables [RhB] and [CT3%] is identified as having a negative effect, highlighting the importance of considering not only the individual effects of variables but also their interactions. Additionally, the [CT3%] is recognized as a significant variable, with a positive effect, suggesting that its presence has a beneficial impact on process efficiency.

Also, in the 3D surface response (Figure 9b) it was possible to verify that RhB removal is maximized near the optimal point of the factorial design [RhB]=100mgL^{-1} and [CT3%]=1gL^{-1}. It is also possible to observe that at high concentrations of RhB, an increase in the photocatalyst concentration (CT3%) results in a slight decrease in RhB removal. Conversely, at low RhB concentrations, an increase in CT3% leads to an increase in RhB removal. This phenomenon can be explained by the fact that in a reaction medium with low RhB concentrations, the increased photocatalyst results in a higher generation of reactive species that will react with the target dye. However, in a medium with high RhB concentration, the dye competes for the absorption of incident photons, causing the increase in photocatalyst concentration not to result in a greater generation of reactive species.

Equation 5 presents the models adjusted by factorial design about the percentage for RhB photodegradation.

$$\text{RhB Removal}(\%) = -46.2250 + 1.4723[\text{RhB}] + 63.5450[\text{CT3\%}] - 0.6527[\text{RhB}][\text{CT3\%}] \quad (5)$$

Table 1. Coded matrix of 2^2 Factorial design for RhB photolysis.

Run	Codified levels		Real variable values		Response variables
	X_1	X_2	$[RhB]_0$ (mg L^{-1})	$[CT3\%]_0$ (g L^{-1})	RhB removal (%)
1	-1	-1	50	1	59.21
					57.39
2	+1	-1	100	1	98.95
					99.61
3	-1	+1	50	2	88.04
					90.38
4	+1	+1	100	2	98.61
					96.5

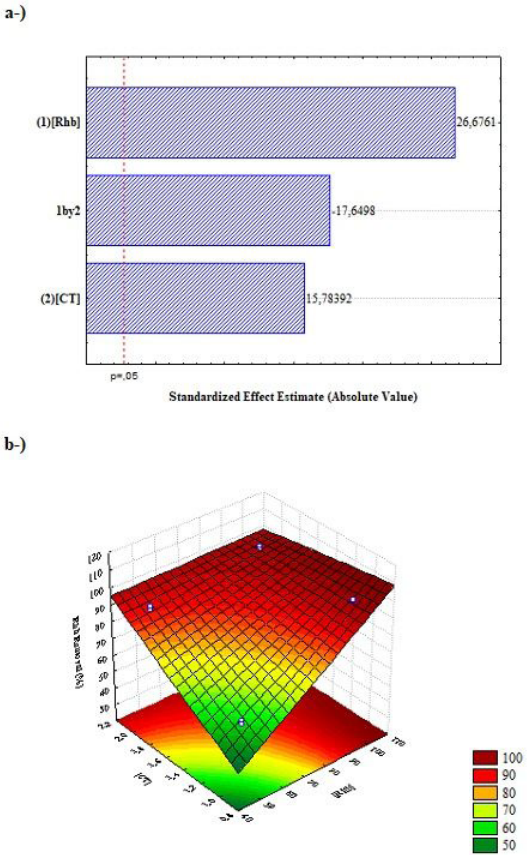

Figure 9. (a) Pareto chart and (b) 3D surface response for RhB photodegradation

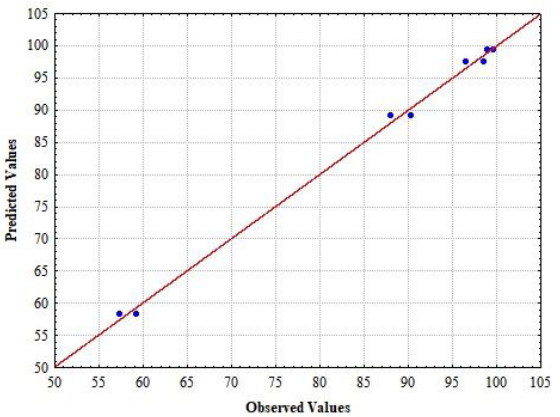

Figure 10. Observed vs predicted values for RhB removal (%).

Figure 10 shows the correlation between the observed and predicted values of the model, and as can be verified, these are very close, indicating an accurate fitting of the model to the experimental data. Consequently, we can assert that the model is useful for explaining the relationship between the independent variables and the response variable.

Figure 11a shows time-concentration profiles for the ideal condition of photocatalysis determined by the experimental design, RhB, and CT3% initial concentrations of 100 mg L^{-1} and 1gL^{-1}, respectively. RhB removal followed apparent first-order decay (k=0.0414 min^{-1}), as indicated by the linear time behavior of ln($[RhB]/[RhB]_0$) over time (Figure 11b).

3.4. Toxicity test

Table 2 presents the results of toxicity assays performed for the best condition studied ([RhB]=100mgL^{-1} and [CT3%] =1 gL^{-1}).

In the analysis of the germination index, it was evident that the untreated raw effluent, containing rhodamine B, exhibited a notably lower value compared to the control, signifying compromised germination when subjected to the pollutant. Conversely, post-treatment, the germination index demonstrated an elevated value, indicative of reduced toxicity in the sample; however, it remained below the germination control threshold.

Concerning the mitotic index, the raw effluent showcased significantly diminished values in comparison to the control, highlighting the inhibitory effect of the contaminant on cell development. Consequently, it is deduced that rhodamine B exerts a toxic impact on Lens culinaris, which is mitigated following treatment.

Our toxicity assays reveal that the treatment process reduces the sample's toxicity but does not eliminate it entirely.

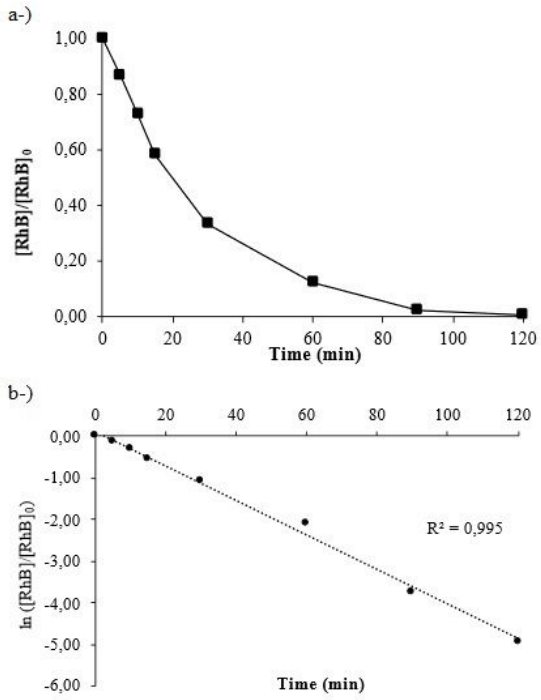

Figure 11. (a) Concentration variation of the RhB during photocatalysis experiment for $[RhB]_0$=100mg L^{-1} and $[CT3\%]_0$=1 gL^{-1} and respective (b) ln ($[RhB]/[RhB]_0$) curve.

Table 2. Mitotic index (MI) and germination index (GI) data on meristems of *Lens culinaris* in samples of effluent treated and not treated.

Assay	MI (%)	GI (%)
Control	25.7 ± 0.01	70
Raw Effluent	15.76 ± 1.41	20
Treated Effluent	32.35 ± 0.98	50

The remaining toxicity can be attributed to to by-products formed during the dye degradation process, which were not mineralized within 120 minutes of treatment.

Mohod et al.[50] observed a delay in the mitotic index of *Lens culinaris* cells when exposed to Rhodamine 6G solution, consistent with the findings of this study. Additionally, Tan et al.[51] also reported a delay in the MI of meristematic cells of *Allium cepa* when exposed to Rhodamine B. Therefore, when plant meristematic cells are exposed to dyes, negative effects are reported, which may be caused by oxidative stress in the cells, thus substantiating the toxicity of dyes[52].

3.5. CT3% recycling

Following the identification of the optimal conditions for RhB photodegradation, the impact of CT3% reuse over four cycles was assessed. As illustrated in Figure 12, the degradation percentage exhibited a decline from 81.98% in cycle I to 25.27% in cycle IV. Moreover, the specific reaction rate (k) decreased from 0.0145 min^{-1} to 0.0025 min^{-1}, likely

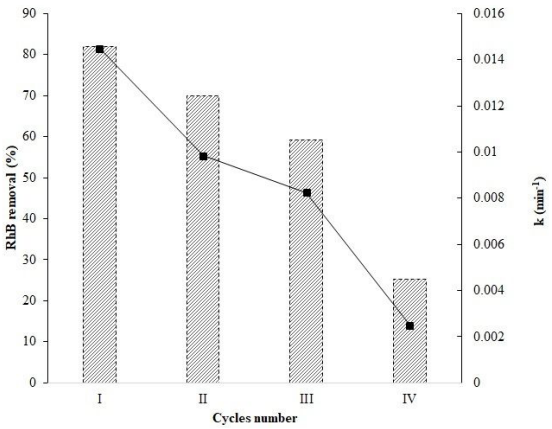

Figure 12. Effect of $CaTiO_3(Ag_{3\%})$ recycling for the RhB photocatalysis.

attributed to the saturation of available active sites. This saturation hindered redox reactions, resulting in a decrease in reactive intermediate species generation, such as hydroxyl radicals (•OH) and superoxide radical anions ($•O_2^-$), thus reducing the photocatalytic activity.

4. Conclusions

The microwave-assisted hydrothermal method proved to be effective in preparing $CaTiO_3$ (CT) and Ag-doped $CaTiO_3$ (CT3% and CT5%) photocatalysts. In all samples, the orthorhombic phase of CaTiO3 was identified by X-ray diffraction, along with a residual phase of TiO_2 (anatase, tetragonal) in the samples containing Ag (CT3% and CT5%), with CT3% exhibiting a more pronounced presence.

Although silver was not directly identified in the diffraction patterns due to its low doping content, a slight peak shift around 2θ = 33° for smaller angles was observed, suggesting the presence of Ag in the CT host lattice. Micro-Raman spectra confirmed the presence of TiO_2 in the anatase phase for CT3% and CT5% samples, while FTIR spectra revealed a distinctive peak at 404 cm^{-1} in the CT3% sample, possibly corresponding to Ti–O vibrations of the TiO_2 phase evident in this sample.

Scanning electron microscopy (SEM) images showed that CT samples predominantly exhibited spherical particle morphology, with some showing a tendency to form edges, resulting in architectures close to cubes or cuboids. Conversely, the addition of 3 mol% and 5 mol% of Ag resulted in particle morphologies with a more cubic and prismatic configuration, with well-defined edges. This morphology alteration may be attributed to both the presence of Ag in the $CaTiO_3$ matrix, influencing morphological formation due to charge imbalance, and the presence of residual TiO_2. In this context, the formation of a $CaTiO_3$-TiO_2 heterojunction is possible, given the similarities between their crystal structures and band arrangements.

Band gap analysis revealed lower values for the silver-doped samples compared to pure CT, with CT3% exhibiting the lowest calculated energy gap. This reduction may be related to the Burstein-Moss effect and the simultaneous presence of the TiO_2 phase in the CT3% sample, may

contribute to this decrease and indicate the formation of a $CaTiO_3$-TiO_2 heterojunction.

Photocatalysis experiments demonstrated that the Rhodamine B degradation performance was significantly enhanced by depositing Ag on the surface of $CaTiO_3$, with higher removal percentages for CT3% and CT5% photocatalysts compared to pure CT. The superior performance of the CT3% photocatalyst is consistent with the characterization of the samples.

Experimental design at two levels revealed that the variables [RhB] and [CT3%] are important and positively contribute to Rhodamine B removal from aquatic environments. It was possible to ascertain that RhB removal is maximized near the optimal point of the factorial design [RhB]=100 mg L^{-1} and [CT3%]=1 g L^{-1}, conditions under which RhB removal followed apparent first-order decay.

Toxicity tests indicated a reduction in the toxicity of the treated samples. However, reuse of CT3% for four cycles demonstrated that the photocatalyst is not stable, with a decrease in dye removal from 81.98% in the first use to 25.27% in the fourth consecutive use, treating Rhodamine B at 100 mg L^{-1}.

These findings can guide the development of more efficient and sustainable photocatalytic materials for treating industrial effluents contaminated with dyes, thereby contributing to environmental preservation and the mitigation of dye pollution impacts.

5. Acknowledgments

Organometallic Catalysis and Materials Laboratory (LaCOM, FCT/Unesp, Brazil), Prope-Unesp (Process no. 9577) and São Paulo Research Foundation (FAPESP) grant number 2019/0696-.

6. References

1. Javaid R, Qazi UY. Catalytic oxidation process for the degradation of synthetic dyes: an overview. Int J Environ Res Public Health. 2019;16(11):2066. http://doi.org/10.3390/ijerph16112066.
2. Rafiq A, Ikram M, Alib S, Niaz F, Khan M, Khan Q, et al. Photocatalytic degradation of dyes using semiconductor photocatalysts to clean industrial water pollution. J Ind Eng Chem. 2021;97:111-28. http://doi.org/10.1016/j.jiec.2021.02.017.
3. Wang H, Li X, Zhao X, Li C, Song X, Zhang P, et al. A review on heterogeneous photocatalysis for environmental remediation: from semiconductors to modification strategies. Chin J Catal. 2022;43(2):178-214. http://doi.org/10.1016/S1872-2067(21)63910-4.
4. Li X, Chen Y, Tao Y, Shen L, Xu Z, Bian Z, et al. Challenges of photocatalysis and their coping strategies. Chemical Catalysis. 2022;2(6):1315-45. http://doi.org/10.1016/j.checat.2022.04.007.
5. Xu D, Ma H. Degradation of rhodamine B in water by ultrasound-assisted TiO2 photocatalysis. J Clean Prod. 2021;313:127758. http://doi.org/10.1016/j.jclepro.2021.127758.
6. Mahendran V, Gogate PR. Degradation of Acid Scarlet 3R dye using oxidation strategies involving photocatalysis based on Fe doped TiO2 photocatalyst, ultrasound and hydrogen peroxide. Separ Purif Tech. 2021;274:119011. http://doi.org/10.1016/j.seppur.2021.119011.
7. Deekshitha VSK, Shetty K V. Solar light active biogenic titanium dioxide embedded silver oxide (AgO/Ag2O@TiO2) nanocomposite structures for dye degradation by photocatalysis. Mater Sci Semicond Process. 2021;132:105923. http://doi.org/10.1016/j.mssp.2021.105923.
8. Ishii T, Anzai A, Yamamoto A, Yoshida H. Calcium zirconate photocatalyst and silver cocatalyst for reduction of carbon dioxide with water. Appl Catal B. 2022;277:119192. http://doi.org/10.1016/j.apcatb.2020.119192.
9. Solís RF, Bedia J, Rodríguez JJ, Belver C. A review on alkaline earth metal titanates for applications in photocatalytic water purification. Chem Eng J. 2021;409:128110. http://doi.org/10.1016/j.cej.2020.128110.
10. Capeli RA, Belmonte T, Caierão J, Dalmaschio CJ, Teixeira SR, Mastelaro VR, et al. Effect of hydrothermal temperature on the antibacterial and photocatalytic activity of WO3 decorated with silver nanoparticles. J Sol-Gel Sci Technol. 2021;97(1):228-44. http://doi.org/10.1007/s10971-020-05433-6.
11. Isik M, Delice S, Gasanly N. Temperature-dependent optical properties of TiO2 nanoparticles: a study of band gap evolution. Opt Quantum Electron. 2023;55(10):905. http://doi.org/10.1007/s11082-023-05138-4.
12. Passi M, Pal B. A review on CaTiO3 photocatalyst: activity enhancement methods and photocatalytic applications. Powder Technol. 2021;388:274-304. http://doi.org/10.1016/j.powtec.2021.04.056.
13. Ernawati L, Wahyuono RA, Widiyandari HW, Risanti DD, Yusariarta AW, Rebeka, et al. Experimental data of CaTiO3 photocatalyst for degradation of organic pollutants (Brilliant green dye)–Green synthesis, characterization and kinetic study. Data Brief. 2020;32:106099. http://doi.org/10.1016/j.dib.2020.106099.
14. Mathiarasu RR, Manikandan A, Panneerselvam K, George M, Raja KK, Almessiere MA, et al. Photocatalytic degradation of reactive anionic dyes RB5, RR198 and RY145 via rare earth element (REE) lanthanum substituted CaTiO3 perovskite catalysts. J Mater Res Technol. 2021;15:5936-47. http://doi.org/10.1016/j.jmrt.2021.11.047.
15. Huang X-J, Yan X, Wu H-Y, Fang Y, Min Y-H, Li H-S, et al. Preparation of Zr-doped CaTiO3 with enhanced charge separation efficiency and photocatalytic activity. Trans Nonferrous Met Soc China. 2016;26(2):464-71. http://doi.org/10.1016/S1003-6326(16)64097-9.
16. Chen M, Xiong Q, Liu Z, Qiu K, Xiao X. Synthesis and photocatalytic activity of Na+ co-doped CaTiO3:Eu3+ photocatalysts for methylene blue degradation. Ceram Int. 2020;46(8):12111-9. http://doi.org/10.1016/j.ceramint.2020.01.256.
17. Chen C, Zhao J, Guo D, Duan K, Wang Y, Lun X, et al. Microwave-assisted synthesis of defective Ca1−xAgxTi1−yCoyO3 with high photoelectrocatalytic activity for organic pollutant removal from water. Dalton Trans. 2022;51(6):2219-25. http://doi.org/10.1039/D1DT03894J.
18. Tanos F, Makhoul E, Nada AA, Bekheet MF, Riedel W, Kawrani S, et al. Graphene oxide-induced CuO reduction in TiO2/CaTiO3/Cu2O/Cu composites for photocatalytic degradation of drugs via peroxymonosulfate activation. Appl Surf Sci. 2024;656:159698. http://doi.org/10.1016/j.apsusc.2024.159698.
19. Yan Y, Yang H, Yi Z, Li R, Xian T. Design of ternary CaTiO3/g-C3N4/AgBr Z-scheme heterostructured photocatalysts and their application for dye photodegradation. Solid State Sci. 2020;100:106102. http://doi.org/10.1016/j.solidstatesciences.2019.106102.
20. Box GEP, Hunter WG, Hunter JS. Statistics for experimenters: an introduction to design, data analysis and model building. New York: Wiley; 1978.
21. Ücker CL, Almeida SR, Cantoneiro RG, Diehl LO, Cava S, Moreira ML, et al. Study of CaTiO3–ZnS heterostructure obtained by microwave-assisted solvothermal synthesis and its application in photocatalysis. J Phys Chem Solids. 2023;172:111050. http://doi.org/10.1016/j.jpcs.2022.111050.
22. Fiskesjö G. The Allium test as a standard in environmental monitoring. Hereditas. 1985;102(1):99-112. http://doi.org/10.1111/j.1601-5223.1985.tb00471.x.

23. Salazar Mercado SA, Quintero Caleño JD, Rojas Suárez JP. Cytogenotoxic effect of propanil using the Lens culinaris Med and Allium cepa L test. Chemosphere. 2020;249:126193. http://doi.org/10.1016/j.chemosphere.2020.126193.
24. Salazar Mercado SA, Caleño JD. Uso de la prueba *Lens culinaris* Med como bioindicador ambiental para identificar el efecto citogenotoxico del pesticida paraquat. Environ Sci Pollut Res Int. 2021;28:37.
25. Salazar Mercado SA, Maldonado Bayona HA. Evaluation of the cytotoxic potential of sodium hypochlorite using meristematic root cells of Lens culinaris Med. Sci Total Environ. 2020;701:134992. http://doi.org/10.1016/j.scitotenv.2019.134992.
26. Lee S-W, Lozano-Sánchez LM, Rodríguez-González V. Green tide deactivation with layered-structure cuboids of Ag/CaTiO3 under UV light. J Hazard Mater. 2013;263(Pt 1):20-7. http://doi.org/10.1016/j.jhazmat.2013.08.017.
27. Cavalcante LS, Marques VS, Sczancoski JC, Escote MT, Joya MR, Varela JA, et al. Synthesis, structural refinement and optical behavior of CaTiO3 powders: a comparative study of processing in different furnaces. Chem Eng J. 2008;143(1-3):299-307. http://doi.org/10.1016/j.cej.2008.05.017.
28. Marques VS, Cavalcante LS, Sczancoski JC, Volanti DP, Espinosa JWM, Joya MR, et al. Influence of microwave energy on structural and photoluminescent behavior of CaTiO3 powders. Solid State Sci. 2008;10(8):1056-61. http://doi.org/10.1016/j.solidstatesciences.2007.11.004.
29. Zheng H, Bagshaw H, Györgyfalva GDCC, Reaney IM, Ubic R, Yerwood J. Raman spectroscopy and microwave properties of CaTiO3–based ceramics. J Appl Phys. 2003;94(5):2948-56. http://doi.org/10.1063/1.1598271.
30. Zheng H, Györgyfalva GDCC, Quimby R, Bagshaw H, Ubic R, Reaney IM, et al. Raman spectroscopy B-site order-disorder in CaTiO3–based microwave ceramics. J Eur Ceram Soc. 2003;23(14):2653-9. http://doi.org/10.1016/S0955-2219(03)00149-3.
31. Moreira ML, Paris EC, Nascimento GS, Longo VM, Sambrano JR, Mastelaro VR, et al. Structural and optical properties of CaTiO3 perovskite-based materials obtained by microwave-assisted hydrothermal synthesis: an experimental and theorical insight. Acta Mater. 2009;57(17):5174-85. http://doi.org/10.1016/j.actamat.2009.07.019.
32. Vemula SK, Katta VS, Ojha S, Singh F, Raav SSK. A study on the Raman response of TiO2 upon ion-implantation and annealing in O2 atmosphere. Opt Mater. 2024;148:114947. http://doi.org/10.1016/j.optmat.2024.114947.
33. Smitha GPS, Gordona KC, Holroydb SE. Raman spectroscopic quantification of calcium carbonate in spiked milk powder samples. Vib Spectrosc. 2013;67:87-91. http://doi.org/10.1016/j.vibspec.2013.04.005.
34. Ševčík R, Mácová P. Localized quantification of anhydrous calcium carbonate polymorphs using micro-Raman spectroscopy. Vib Spectrosc. 2018;95:1-6. http://doi.org/10.1016/j.vibspec.2017.12.005.
35. Karthikeyan C, Thamima M, Karuppuchamy S. Dye removal efficiency of perovskite structured CaTiO3 nanospheres prepared by microwave assisted method. Mater Today Proc. 2021;35:44-7. http://doi.org/10.1016/j.matpr.2019.05.421.
36. Rai AK, Rao KN, Kumar LV, Mandal KD. Synthesis and characterization of ultra fine barium calcium titanate, barium strontium titanate and Ba1-2xCaxSrxTiO3 (x = 0.05-0.10). J Alloys Compd. 2009;475:16-320. http://doi.org/10.1016/j.jallcom.2008.07.038.
37. Patil SK, Shah N, Blum FD, Kahaman MN. Fourier transform infrared analysis of hydroxyl content of hydrothermally processed heteroepitaxial barium titanate films. J Mater Res. 2005;20(12):3312-9. http://doi.org/10.1557/jmr.2005.0406.
38. Stoyanova D, Stambolova I, Blaskov V, Zaharieva K, Avramova I, Dimitrov O, et al. Mechanical milling of hydrothermally obtained CaTiO3 powders-morphology and photocatalytic activity. Nano-Structures & Nano-Objects. 2019;18:100301. http://doi.org/10.1016/j.nanoso.2019.100301.
39. Li Y, Zhang F. Self-assembly of perovskite nanocrystals: from driving forces to applications. J Energy Chem. 2024;88:561-78. http://doi.org/10.1016/j.jechem.2023.09.048.
40. Souza AE, Moreira ML, Volanti DP, Paris EC, Teixeira SR, Longo E. Morphological and structural changes of CaxSr1-xTiO3 powders obtained by the microwave-assisted hydrothermal method. Int J Appl Ceram Technol. 2012;9(1):186-92. http://doi.org/10.1111/j.1744-7402.2011.02648.x.
41. Souza AE, Teixeira SR, Morilla-Santos C, Schreiner WH, Filho PNL, Longo E. Photoluminescence activity of Ba1-xCaxTiO3: dependence on particle size and morphology. J Mater Chem C Mater Opt Electron Devices. 2014;2(34):7056-70. http://doi.org/10.1039/C4TC00897A.
42. Mazzo T, Libanori GSN, Moreira ML, Avansi W Jr, Mastelaro VR, Varela JA, et al. Influence of titanium precursor on photoluminescence mission of micro-cube-shaped CaTiO3. J Lumin. 2015;165:130-7. http://doi.org/10.1016/j.jlumin.2015.03.028.
43. Jana A, Meena A, Patil SA, Jo Y, Cho S, Park Y, et al. Self-assembly of perovskite nanocrystals. Prog Mater Sci. 2022;129:100975. http://doi.org/10.1016/j.pmatsci.2022.100975.
44 Lin J, Hu J, Qiu C, Huang H, Chen L, Xie Y, Zhang Z, Lin H, Wang X. In situ hydrothermal etching fabrication of CaTiO3 on TiO2 nanosheets with heterojunction effects to enhance CO2 adsorption and photocatalytic reduction. Catal Sci Technol. 2019;9:336-46. http://doi.org/10.1039/C8CY02142B.
45. Wood DL, Tauc J. Weak absorption tails in amorphous semiconductors. Phys Rev, B, Solid State. 1972;5(8):3144-51. http://doi.org/10.1103/PhysRevB.5.3144.
46. Xie J, Ye Q, Zhou J, Liao Y, Qian G. The photocatalytic activity of CaTiO3 derived from the microwave-melting heating process of blast furnace slag. Nanomaterials (Basel). 2023;13(8):1412. http://doi.org/10.3390/nano13081412.
47. Sun R, Wang Z, Saito M, Shibata N, Ikuhara Y. Atomistic mechanisms of nonstoichiometry-induced twin boundary structural transformation in titanium dioxide. Nat Commun. 2015;6(1):7120. http://doi.org/10.1038/ncomms8120.
48. Bai L, Xu Q, Cai Z. Synthesis of Ag@AgBr/CaTiO3 composite photocatalyst with enhanced visible light photocatalytic activity. J Mater Sci Mater Electron. 2018;29(20):17580-90. http://doi.org/10.1007/s10854-018-9861-y.
49. Passi M, Pal B. Influence of Ag/Cu photodeposition on CaTiO3 photocatalytic activity for degradation of Rhodamine B dye. Korean J Chem Eng. 2022;39(4):942-53. http://doi.org/10.1007/s11814-021-0975-1.
50. Mohod AV, Clemente DB, Klanovicz N, Moreira PF, Bagal MV, Teixeira ACS, et al. Degradation of Rhodamine 6G dye using a novel glass-marble packed bed reactor-based cavitation. Chem Eng Process. 2023;184:109287. http://doi.org/10.1016/j.cep.2023.109287.
51. Tan D, Bai B, Jiang D, Shi L, Cheng S, Tao D, et al. Rhodamine B induces long nucleoplasmic bridges and other nuclear anomalies in Allium cepa root tip cells. Environ Sci Pollut Res Int. 2014;21(5):3363-70. http://doi.org/10.1007/s11356-013-2282-9.
52. Klanovicz N, Stefanski FS, Camargo AF, Michelon W, Treichel H, Silva Costa Teixeira AC. Complete wastewater discoloration by a novel peroxidase source with promising bioxidative properties. J Chem Technol Biotechnol. 2022;97(9):2613-25. http://doi.org/10.1002/jctb.7134.